IEEE Access
Multidisciplinary | Rapid Review | Open Access Journal

Received May 19, 2020, accepted June 17, 2020, date of publication June 22, 2020, date of current version July 2, 2020.

Digital Object Identifier 10.1109/ACCESS.2020.3004136

The Level-Set Method for Multi-Material Wet Etching and Non-Planar Selective Epitaxy

ALEXANDER TOIFL[1], MICHAEL QUELL[1], XAVER KLEMENSCHITS[2], PAUL MANSTETTEN[2], ANDREAS HÖSSINGER[3], SIEGFRIED SELBERHERR[2], (Fellow, IEEE), AND JOSEF WEINBUB[1], (Member, IEEE)

[1]Christian Doppler Laboratory for High Performance TCAD, Institute for Microelectronics, TU Wien, 1040 Wien, Austria
[2]Institute for Microelectronics, TU Wien, 1040 Wien, Austria
[3]Silvaco Europe Ltd., Cambridge PE27 5JL, U.K.

Corresponding author: Alexander Toifl (alexander.toifl@tuwien.ac.at)

The financial support by the Austrian Federal Ministry for Digital and Economic Affairs and the National Foundation for Research, Technology and Development is gratefully acknowledged. The authors acknowledge TU Wien University Library for financial support through its Open Access Funding Program.

ABSTRACT We present numerical methods to enable accurate and robust level-set based simulation of anisotropic wet etching and non-planar epitaxy for semiconductor fabrication. These fabrication techniques are characterized by highly crystal orientation-dependent etch/growth rates, which lead to non-convex Hamiltonians in their description by the level-set equation. As a consequence, instable surface propagation may emerge, leading to unphysical results. We propose a calibration-free Stencil Lax-Friedrichs scheme and an advanced adaptive time-stepping approach, tailored to the level-set speed functions associated with anisotropic etching and epitaxy. The scheme calculates the numerical dissipation based on information about the local geometry and the nature of the etch rates/growth function, which enables an optimized trade-off between overly rounding of sharp geometric features and stable surface propagation. Furthermore, we introduce the deposition top layer method, which allows for robust handling of multiple material regions in non-planar epitaxy simulations. Both methods are demonstrated in a prototypical implementation, which is used to validate the capability and accuracy of our approaches. In particular, two-dimensional wet etching and three-dimensional epitaxy simulations are performed and characteristic geometry parameters are compared to the ideally expected values, showing robustness and high accuracy.

INDEX TERMS Crystallographic etching, non-planar epitaxial growth, level-set method, non-convex Hamiltonian, multi-material simulation.

I. INTRODUCTION

Fabrication techniques which exploit the crystalline nature of semiconductor materials are highly important for cutting-edge semiconductor technologies to enable intricate device geometries. A widely used technique is the anisotropic wet etching of silicon (Si), where wet etchants (e.g., potassium hydroxide (KOH)) are used to remove the substrate with highly different rates, depending on the crystallographic direction of the etched material. The final geometry is characterized by slowly etching crystallographic planes (i.e., facets), which allows for predictable and precise topographies. While anisotropic wet etching is the traditional fabrication technique for cavities in microelectromechanical systems (MEMS) [1] (Fig. 1a), further applications include patterned sapphire substrates for gallium nitride-based light emitting diodes [2] and source-drain engineering for metal-oxide-semiconductor field-effect transistors (MOSFETs) on the nanoscale [3], [4]. A similar fabrication process is epitaxial growth of Si or silicon-germanium (SiGe) on non-planar substrates (Fig. 1b). In order to enhance the device characteristics of advanced-node semiconductor devices (e.g., FinFETs [5] and stacked nanosheet devices [6], [7]), the exact geometry of epitaxially grown Si or SiGe is crucial.

Both anisotropic etching and non-planar epitaxy require precise control of the final topography. In the presence of complex three-dimensional device geometries, it is beneficial to guide the fabrication process with topography simulation beforehand. Level-set methods, first presented by Osher and Sethian [8], are particularly well suited to track the evolution of the wafer surface, in particular, when topological changes are expected [9]. The level-set method is based on

The associate editor coordinating the review of this manuscript and approving it for publication was Jiang Wu.

This work is licensed under a Creative Commons Attribution 4.0 License. For more information, see https://creativecommons.org/licenses/by/4.0/

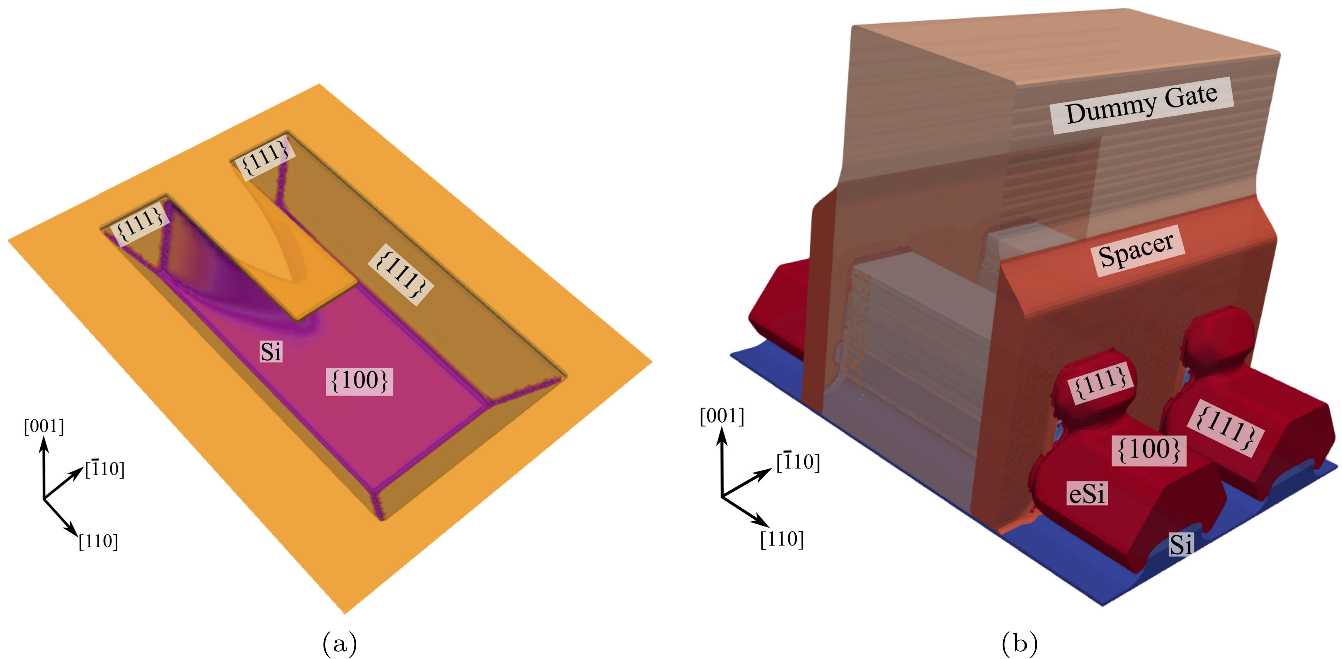

FIGURE 1. **(a) Cavity etch producing a free cantilever for sensor applications. The Si substrate is anisotropically etched with a wet etchant, e.g., KOH. The etch rates along the ⟨111⟩ direction are significantly smaller than the rates along ⟨100⟩, resulting in a topography defined by {111} planes.**
(b) Advanced-node stacked nanosheet geometry with epitaxially grown source and drain (red). Silicon crystal facets are labeled, showing the resulting complex geometries due to the epitaxial growth [6], [7].

the description of a surface in the simulation domain Ω by the zero level-set $\{x \in \Omega \,|\, \phi(x) = 0\}$ of the level-set function ϕ. The temporal evolution of the surface (also referred to as front) is determined by the level-set equation [10]

$$\frac{\partial \phi}{\partial t} + H(\nabla \phi) = 0, \tag{1}$$

which assumes the form of a Hamilton-Jacobi equation. The corresponding Hamiltonian $H = V\|\nabla\phi\|$, where $\|\cdot\|$ denotes the Euclidean norm, comprises a general speed function V which determines the propagation of the front.

V introduces the information about the physical process which enforces the change of the surface topography. Anisotropic etch and growth processes are characterized by etch/growth rates along certain crystallographic directions. These rates are known from experiments to primarily depend on the involved materials/etchants and on the process temperature [11]–[13]. Speed functions V that reflect the experimental observations give rise to a non-convex Hamiltonian [15], causing numerical problems at sharp corners.

The discretized level-set function inevitably introduces inaccuracies in the calculation of the normal vector of the front. Combined with the highly orientation-sensitive speed function, instable front propagation and thus unphysical results may emerge. The discretized level-set equation can be stabilized by introducing numerical dissipation, which results in dissipative schemes, such as the Lax-Friedrichs scheme [16]. The additional numerical dissipation terms have the detrimental effect of artificially rounding sharp geometrical features. Thus, in order to achieve stability and sharp geometrical features, it is essential to add the appropriate amount of numerical dissipation. In the case of speed functions which can be analytically described, the appropriate dissipation can be exactly calculated from the derivative of the Hamiltonian [14]. In contrast, for general etching and growth processes the speed function is not explicitly given. Hence, the dissipation coefficients can be heuristically chosen [17], or a numerical approximation of the derivative of the Hamiltonian is employed, as proposed by Montoliu *et al.* [18]. However, the approximation presented by Montoliu *et al.* requires a numerical calibration parameter which has to be determined for every etching/growth condition. In this work, we present a method to calculate the numerical dissipation based on the *nature* of the speed function V and the local geometry while not resorting to calibration parameters. Furthermore, advanced adaptive time-stepping based on the introduced numerical dissipation is employed. As a result, the time step is appropriately chosen to enable a stable front propagation.

The high orientation sensitivity of wet etching and epitaxy processes requires an accurate description of the zero level-set. The local geometry is well known to play a decisive role in anisotropic processing techniques, in particular in the field of epitaxy [19], [20]. Furthermore, in a semiconductor process simulation, multiple material regions are present and the level-set framework must handle material interfaces and thin layers robustly. Multi-level-set approaches have been demonstrated to enable robust etching simulations [21] and enable sub grid cell resolution for thin layers.

However, commonly used multi-level set approaches for etching simulations are not suitable for selective growth

processes due to the way the material regions are additively represented. As a consequence, the local convexity in some regions is artificially altered, resulting in non-physical growth. In this work, we propose the introduction of a deposition top level-set function (*deposition top layer*), which allows for robust and accurate simulations of anisotropic epitaxy processes on non-planar substrates.

Our calibrarion-free Stencil Lax-Friedrichs scheme as well as our multi-material scheme for selective deposition are demonstrated with a prototypical implementation based on the open source topography simulator `ViennaTS` [22].

This paper is organized as follows. In Section II we derive our proposed numerical dissipation scheme for robust modeling of anisotropic etching and growth. Section III presents our multi-level-set scheme to robustly model selective deposition processes with sub grid resolution. In Section IV the simulation setups and expected results are introduced. Section V discusses results for these setups using our proposed methods.

II. NUMERICAL DISSIPATION SCHEME

During an anisotropic process step, the crystalline nature of the processed materials gives rise to strongly crystallographic orientation-dependent etch rates. The kinetics of the chemical reactions during etching or deposition establish significantly differing etch/growth rates depending on the exposed crystal facet [11]. Consequently, the speed function V is a function of the surface normal vector, which locally defines the exposed crystallographic directions. During a typical wet etching step, the chemical properties of the etchant are actively controlled to be uniform (e.g., by means of stirring) and the temperature is held constant [12]. Under these conditions, we can neglect the local impact of reactant transport[1] on the etching kinetics. Consequently, the etch rate only depends on the exposed crystallographic planes, resulting in a speed function (2) which is a function of the local surface normal vector $\vec{n} = [n^x, n^y, n^z]^T$

$$V = V(n^x, n^y, n^z). \tag{2}$$

In general, (2) implies a temporal evolution of the surface driven by the surface's geometry with no further *external* driving force. Etch and growth rates are typically measured for certain crystallographic directions, given by Miller indices (e.g., $\langle 100\rangle$, $\langle 111\rangle$). In order to calculate the corresponding rate for a general local surface normal, interpolation between the measured rates for a set of given orientations is required. Gosálvez *et al.* [25] presented a comprehensive study on the quality of different schemes (trilinear, triquadratic, etc.) specifically for wet etching of Si. However, in the case of selective epitaxy, deposition rates are usually only measured for three or four crystal directions. Therefore, one can employ linear interpolation while accounting for the symmetry introduced by the cubic crystal structure of Si, as proposed by Hubbard [26]. Fig. 2 shows typical anisotropic speed functions associated with etching and epitaxy. These speed functions show the characteristically high ratio of maximum and minimum speed values, which causes the issue of numerical stability discussed in this work.

Within the level-set framework the surface normals are calculated from the level-set function ϕ

$$\vec{n} = \frac{\nabla\phi}{\|\nabla\phi\|}. \tag{3}$$

Consequently, the speed function and the resulting Hamiltonian are a function of the spatial derivatives of the level-set function ϕ_p, $p \in \{x, y, z\}$

$$H = V\|\nabla\phi\| = V(\vec{n}(\phi_x, \phi_y, \phi_z))\|\nabla\phi\|. \tag{4}$$

In general, the Hamiltonian $H(\phi_x, \phi_y, \phi_z)$ is non-convex, because the formal convexity condition

$$\frac{\partial^2 H}{\partial\phi_p\partial\phi_q} \geq 0 \quad p, q \in \{x, y, z\}, \tag{5}$$

where ϕ_p refers to the partial derivative of ϕ with respect to the spatial coordinate p, is not fulfilled. The non-convex nature of the Hamiltonian is problematic if the front has sharp corners. Along a front with high curvature (as depicted in Fig. 3a) a non-convex speed function $V(\vec{n})$ (illustrated in the inset) is characterized by possibly multiple extrema. Due to the limited spatial resolution, the speed of the front between two grid points has to be estimated by a combination of the speed at exactly these two grid points [15]. However, it is not straightforward to choose a high quality combination, because on the one hand the exact magnitude of the extrema (c.f., Fig. 2) and on the other hand the spatial resolution must be considered. Furthermore, after a time step Δt the front has propagated by a small distance resulting in a new set of front speed values at the grid points. Even though the global shape of the corner does not significantly change during Δt, the set of front speed values associated with the spatially constant grid points can be considerably different. If the speed function of a certain grid point is changing considerably between two time steps, the local advection speed might change significantly in each time step. This situation is illustrated in Fig. 3a, where the speed function takes values close to the maximum value along $\langle 113\rangle$. Depending on the alignment of the front relative to the grid points, the directions of the surface normals vary slightly, resulting in considerably different speed values assigned to the grid points. As a consequence, high frequency disturbances on the scale of spatial resolution occur, resulting in propagating unphysical oscillations of the level-set function, which detrimentally affect the global solution.

In the case of etching and epitaxial growth simulations, the front generally evolves towards individual sharp corners, i.e., planes forming the crystallographic facets. These regions are depicted in Fig. 3b. While the speed values associated with the active grid points (i.e., grid points close to the surface, which are visited to solve the level-set equation) are small and well-behaved, the sharp corners cause instable propagation, which results in overly high etch or growth rates and thus

[1] A reactant transport model would introduce dependencies on flux distributions, reactant adsorption/desorption, and particle (re-) emission.

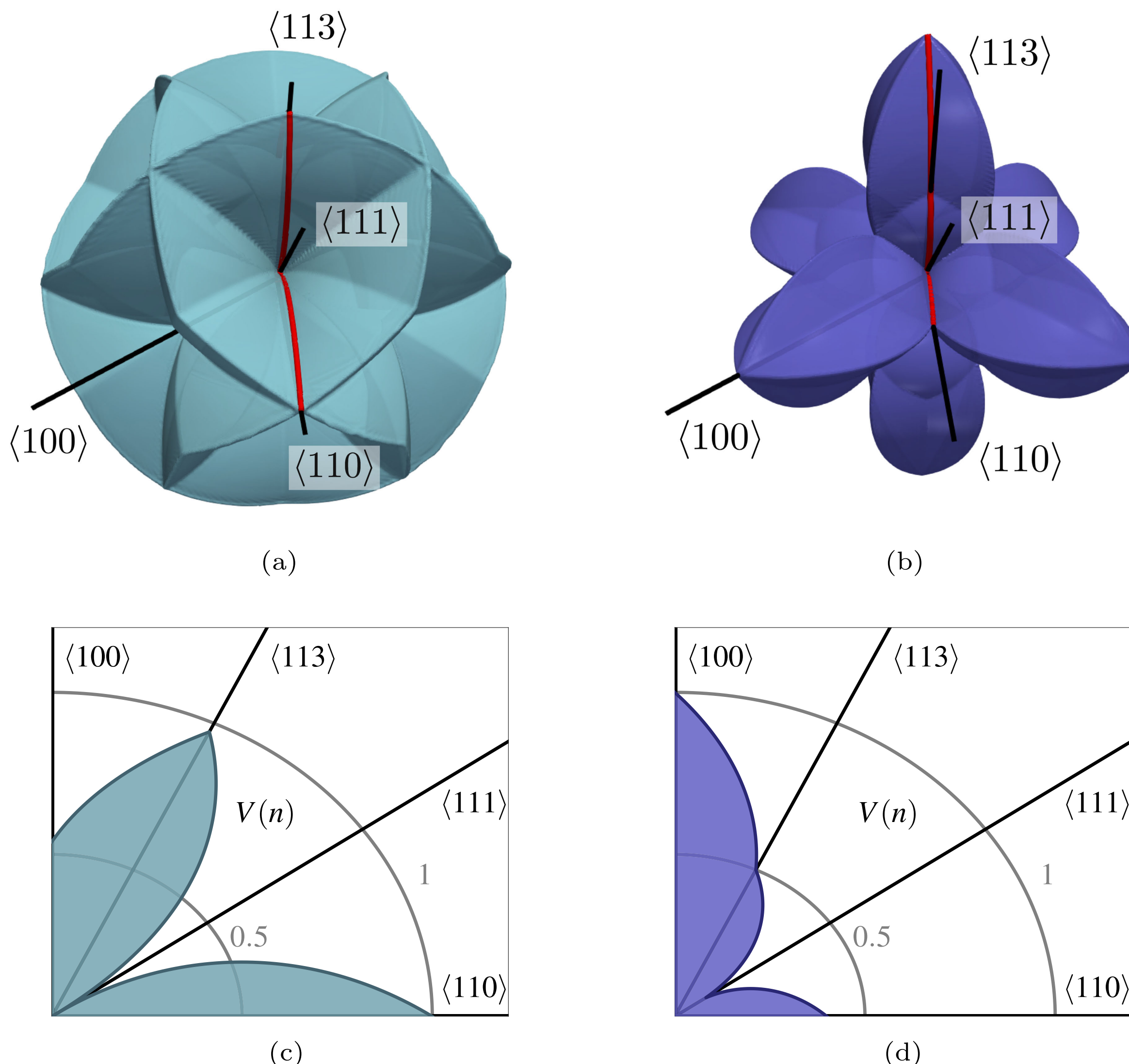

FIGURE 2. Typical etching and growth rate distributions for cubic crystals. (a) and (b) Illustration of the three-dimensional distributions and slice paths (red line). (c) and (d) Visualization of the rates along the slice paths. The distribution functions originate from linear interpolation between the crystallographic directions ⟨100⟩, ⟨110⟩, ⟨113⟩, and ⟨111⟩. The ⟨·⟩ notation refers to the set of equivalent directions in the cubic crystal structure. Both distributions are characterized by a global minimum at ⟨111⟩ direction resulting in slowly moving {111} planes.

leads to physically wrong results. In order to overcome this problem, we employ the technique of artificially smoothing out corners [16] and present in the next section a numerical dissipation scheme which takes the *nature* of $V(\vec{n})$ (i.e, the form and smoothness of $V(\vec{n})$, as depicted in Fig. 2) into account.

A. STENCIL LOCAL LAX FRIEDRICHS NUMERICAL DISSIPATION SCHEME

Anisotropic etch and growth simulation discussed in this work naturally involves sharp corners, which result in non-differentiable level-set fields. Consequently, the physically relevant solution of the level-set equation is not smooth and it is necessary to solve (1) in a more general way, resulting in the so-called viscosity solution. The viscosity solution is defined as the weak solution to a partial differential equation and is obtained by the vanishing viscosity method [27]. A numerical scheme which employs this idea is the monotone Lax-Friedrichs scheme, originally introduced by Crandall and Lions [28]. The Lax-Friedrichs scheme is first-order in space and is characterized by an additional linear numerical dissipation term. For every active grid point P, the Hamiltonian in (1) is replaced by the numerical Hamiltonian

$$\hat{H} = H\left(\frac{\phi_x^- + \phi_x^+}{2}, \frac{\phi_y^- + \phi_y^+}{2}, \frac{\phi_z^- + \phi_z^+}{2}\right) - \sum_{l\in\{x,y,z\}} \alpha^l \left(\frac{\phi_l^+ - \phi_l^-}{2}\right), \quad (6)$$

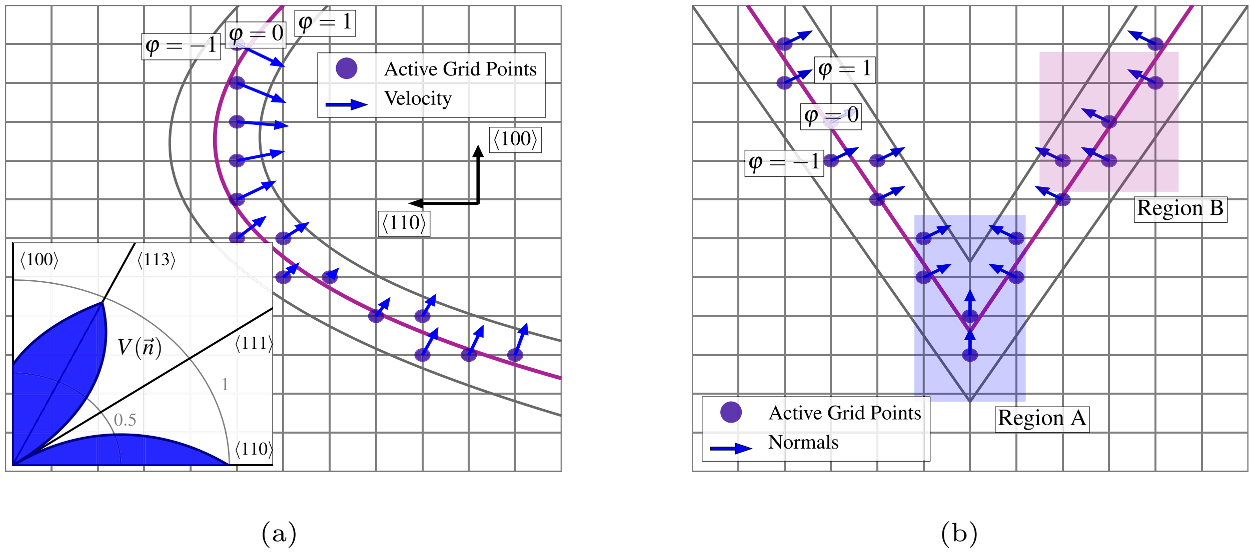

FIGURE 3. (a) Highly anisotropic etch rates (inset) induce spatially strongly varying speed values assigned to active grid points. (b) A typical wet etching simulation generates sharp corners (Region A) and flat surfaces (Region B).

where ϕ_l^+ refers to the first-order forward and ϕ_l^- to the backward discretization of the spatial derivative with respect to $l \in \{x, y, z\}$. The dissipation coefficients α^l are associated with P and define the cumulated numerical dissipation

$$D = \sum_{l \in \{x,y,z\}} \alpha^l \left(\frac{\phi_l^+ - \phi_l^-}{2} \right), \tag{7}$$

which allows to write the numerical Hamiltonian $\hat{H}$ in a compact form as the difference of the Hamiltonian and numerical dissipation.

$$\hat{H} = H\left(\phi_l^+, \phi_l^-\right) - D\left(\phi_l^+, \phi_l^-\right) \quad l \in \{x, y, z\} \tag{8}$$

The numerical dissipation is designed to be non-zero in regions where the level-set function varies abruptly (e.g., sharp edges of the interface). Crandall and Lions proved in 1984 that the first-order Lax-Friedrichs scheme, defined by the explicit Euler time integration

$$\phi^{t+\Delta t} = \phi^t - \Delta t \hat{H}\left(\phi_l^-, \phi_l^+\right) \quad l \in \{x, y, z\} \tag{9}$$

with the numerical Hamiltonian (8), is stable if the scheme is monotone [28]. Therefore, it is possible to estimate the general bounds of the dissipation coefficients α^l: The Lax-Friedrichs scheme is stable if it is non-decreasing in every argument $\phi_{i,j,k}$, $\phi_{i\pm1,j,k}$, $\phi_{i,j\pm1,k}$, and $\phi_{i,j,k\pm1}$, where i, j, and k refer to the grid point indices.

$$\frac{\mathrm{d}\phi_{i,j,k}^{t+\Delta t}}{\mathrm{d}\phi_{i,j,k}^{t}} \geq 0 \quad \Rightarrow \quad \Delta t \left(\frac{\alpha^x}{\Delta x} + \frac{\alpha^y}{\Delta y} + \frac{\alpha^z}{\Delta z} \right) \leq 1 \tag{10}$$

$$\frac{\mathrm{d}\phi_{i,j,k}^{t+\Delta t}}{\mathrm{d}\phi_{i\pm1,j,k}^{t}} \geq 0 \quad \Rightarrow \quad \alpha^x \geq \left| \frac{\partial H}{\partial \phi_x} \right| \tag{11}$$

$$\frac{\mathrm{d}\phi_{i,j,k}^{t+\Delta t}}{\mathrm{d}\phi_{i,j\pm1,k}^{t}} \geq 0 \quad \Rightarrow \quad \alpha^y \geq \left| \frac{\partial H}{\partial \phi_y} \right| \tag{12}$$

$$\frac{\mathrm{d}\phi_{i,j,k}^{t+\Delta t}}{\mathrm{d}\phi_{i,j,k\pm1}^{t}} \geq 0 \quad \Rightarrow \quad \alpha^z \geq \left| \frac{\partial H}{\partial \phi_z} \right| \tag{13}$$

This set of inequalities determines the conditions on the dissipation coefficients ensuring a stable Lax-Friedrichs scheme and has to be fulfilled at every grid point P. The first inequality (10) states that there is an upper bound for the dissipation coefficients, which is further discussed in Section II-B. The remaining inequalities indicate a relation between the dissipation coefficients and the partial derivatives $\frac{\partial H}{\partial \phi_l}$, $l \in \{x, y, z\}$, which one can calculate for a purely surface normal-dependent Hamiltonian (4), employing the chain rule of differentiation, as presented in the Appendix.

$$\frac{\partial H}{\partial \phi_l} = \frac{\partial V}{\partial n^l} \frac{\phi_p^2 + \phi_q^2}{\|\nabla\phi\|^2} - \frac{\partial V}{\partial n^p} \frac{\phi_p \phi_l}{\|\nabla\phi\|^2} - \frac{\partial V}{\partial n^q} \frac{\phi_q \phi_l}{\|\nabla\phi\|^2} + V n^l$$
$$l, p, q \in \{x, y, z\}, \; l \neq p \neq q \tag{14}$$

(14) consists of a constant velocity term Vn^l and three terms involving $\partial V/\partial n^l$. The former is present even for constant $V(\vec{n}) = V_0$ [16], while the latter considers the local *nature* of the $V(\vec{n})$ and the local geometry described by ϕ.

In order to allow for a $V(\vec{n})$ of any complexity, $\partial V/\partial n^l$ can be calculated numerically with a central difference scheme proposed by Montoliu *et al.* [18]

$$\frac{\partial V}{\partial n^x} = \frac{V(n^x + \Delta N, n^y, n^z) - V(n^x - \Delta N, n^y, n^z)}{2\Delta N} \tag{15}$$

and similar terms for $\frac{\partial V}{\partial n^y}$ and $\frac{\partial V}{\partial n^z}$. We use $\Delta N = \varepsilon^{\frac{1}{3}} V$, with ε referring to the floating point accuracy, which balances the truncation and roundoff error [29].

It is critical to choose the correct amount of numerical dissipation, because pronounced dissipation causes oversmoothing of the numerical solution of the Hamilton-Jacobi equation. In the literature, several variations of the

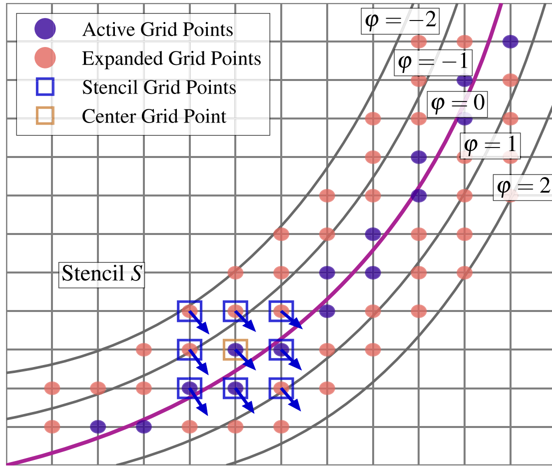

FIGURE 4. The Stencil Lax-Friedrichs scheme (16) employs the stencil S in order to calculate the dissipation coefficients for every active grid point.

Lax-Friedrichs scheme have been studied, which provide various degrees of trade-off between instable front propagation and over-smoothing. The approaches range from employing the worst-case dissipation coefficients $\alpha^l = \frac{\partial H}{\partial \phi_l}$ found in the *entire domain* [18] to only using the grid point which is currently processed [16]. Furthermore, the final terms for α^l have been proposed to contain calibration factors which are specifically determined for certain speed functions [17], [18], or making use of analytical expressions [14].

We propose a scheme for the calculation of the dissipation coefficients at grid point P, which is based on the Stencil Lax-Friedrichs flux [16] and incorporates (14) and (15).

$$\alpha^l = \max_{P \in S} \left| \frac{\partial V}{\partial n^l} \frac{\phi_p^2 + \phi_q^2}{\|\nabla \phi\|^2} - \frac{\partial V}{\partial n^p} \frac{\phi_p \phi_l}{\|\nabla \phi\|^2} - \frac{\partial V}{\partial n^q} \frac{\phi_q \phi_l}{\|\nabla \phi\|^2} + V n^l \right|, \quad l, p, q \in \{x, y, z\},\ l \neq p \neq q \tag{16}$$

S denotes a stencil composed of grid points around the currently processed center grid point P. Fig. 4 illustrates the stencil, which is considered for every active grid point. In order to calculate α^l, (14) and (15) are evaluated at 9 and 27 grid points for two- and three-dimensional simulation, respectively. The evaluation of α^l on S requires level-set values on grid points which are not in close proximity to the surface. These grid points are referred to as *expanded* grid points. By using local information via the rectangular stencil, a trade-off between numerical stability and overly rounding of corners is achieved. While only considering the center grid point might result in insufficient dissipation, evaluating α^l for a larger number of grid points might cause non-physical rounding.

Fig. 5 visualizes the dissipation scheme for a two-dimensional V-shaped geometry (cf. Fig. 3b). The dissipation coefficients α^x and α^y are depicted in Fig. 5a and Fig. 5b, respectively, and are characterized with values close to zero in the flat regions and larger values in the proximity of the corner. Consequently, the corresponding numerical dissipation shown in Fig. 5c, is non-zero around the corner. The dissipation values cancel out the artificially high values imposed by the Hamiltonian (Fig. 5d). Hence, the resulting numerical Hamiltonian (8) effectively reduces the impact of the non-convex speed function and enables front propagation with the corrected speed of the predominating facets.

B. STENCIL LAX-FRIEDRICHS SCHEME WITH ADVANCED ADAPTIVE TIME STEPPING

The Stencil Lax-Friedrichs scheme (16) is consistent with (11)-(13). In order to ensure monotonicity, it is essential that (10) has to be fulfilled as well. (10) assumes a form which is very similar to the Courant-Friedrichs-Lewy (CFL) condition [30]. The dissipation coefficients are related to the temporal and spatial resolution, such as the front speed is related to these quantities in the traditional CFL condition. Unlike in the traditional case, there is no parameter analogous to the CFL number.

In order to ensure the additional monotonicity condition, (10) is checked for every grid point P processed (i.e., active grid point in the sparse-field level-set implementation). If (10) is violated, a new time step Δt_n is consistently chosen according to

$$\Delta t_n = \min_{P \in N} \left(\frac{\alpha^x}{\Delta x} + \frac{\alpha^y}{\Delta y} + \frac{\alpha^z}{\Delta z} \right)^{-1}, \tag{17}$$

where N refers to the set of active grid points. Δt_n is typically smaller than the time step indicated by the traditional CFL condition. Thus, it is possible to ensure a stable numerical scheme, by fulfilling both the CFL and the monotonicity condition (10).

In conclusion, for a speed function V of the form (2) we construct a Stencil Lax-Friedrichs scheme with monotonicity preserving dissipation coefficients (16) and time steps (17). The scheme does not rely on calibration factors and thus can be employed for general speed functions which are purely surface normal-dependent. The numerical stabilization achieved by the Stencil Lax-Friedrichs scheme and the time-stepping thus enable the simulation of complex anisotropic processes.

III. MULTI-LEVEL-SET SCHEME FOR NON-PLANAR EPITAXY

In topography simulations different materials with disparate front propagation properties can be present. Within a level-set framework multiple material regions can be treated by defining multiple level-sets. A robust multi-material representation, which enables the resolution of thin material regions (i.e., thickness below the grid-spacing), has been presented by Ertl and Selberherr [21]. The representation is based on additive layers generated from sequential union operations. Given a stack of K materials, represented by the individual enclosing volumes $\mathcal{M}_k$, the j-th layer L_j is

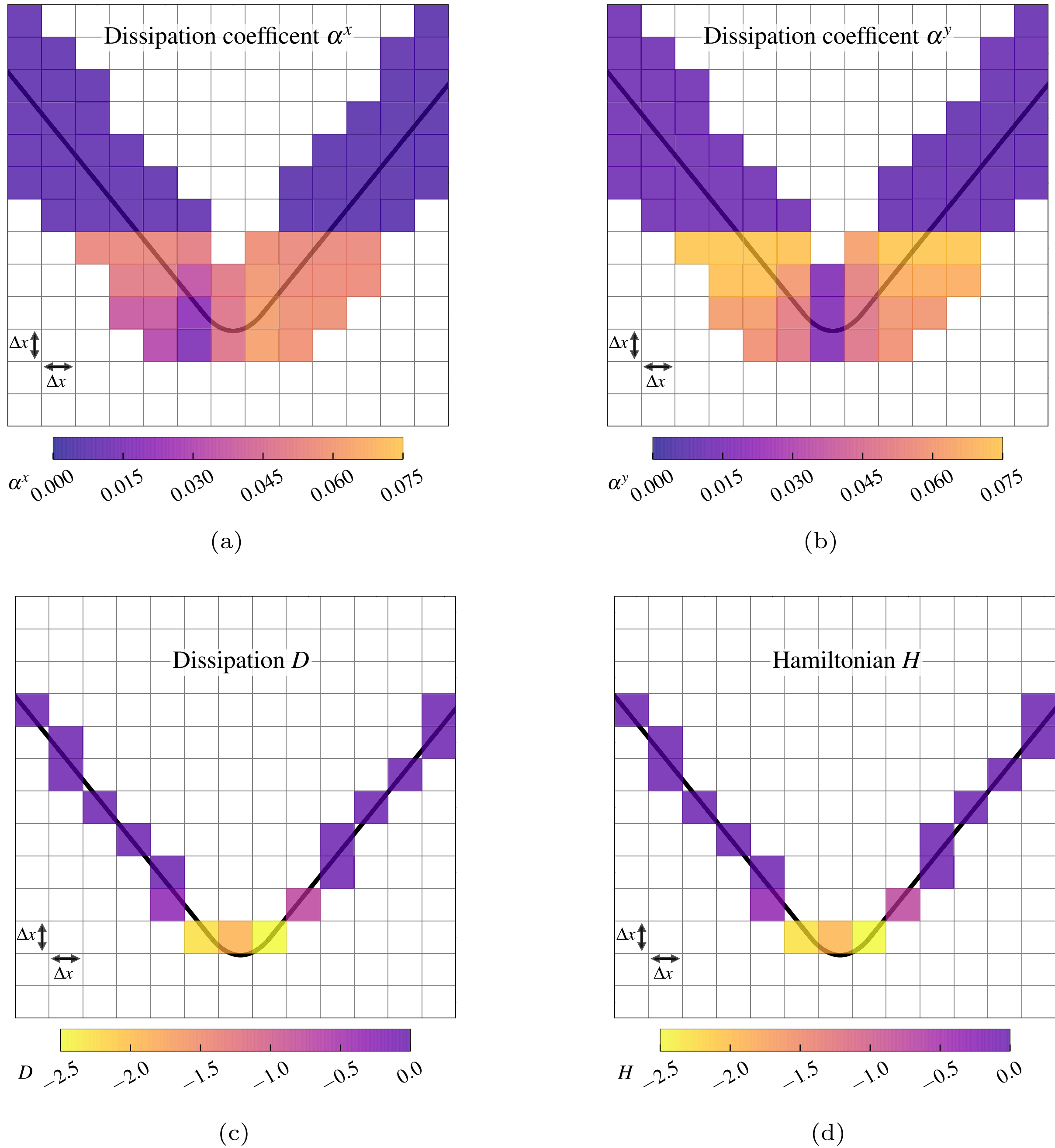

FIGURE 5. Dissipation coefficients (a) α^x and (b) α^y calculated for a V-shaped front (solid line). In the flat regions, the coefficients are close to zero, while they reach their maximum values in proximity of the sharp corner. The resulting numerical dissipation (c) balances the artificially elevated values of the Hamiltonian (d) close to the corner. The resulting numerical Hamiltonian ($H - D$) yields the small values associated with the flat regions for all active grid points, which enables a stable front propagation.

defined as

$$\mathrm{L}_j = \bigcup_{k=1}^{j} \mathcal{M}_k. \tag{18}$$

The topmost layer L_K unites all underlying materials and thus is called *top layer* (TL). The level-set approach enables the calculation of Boolean operations by employing minimum and maximum operations on the level-set functions. Furthermore, the individual material regions are reconstructed from the layers with sequential set-difference operations.

When treating multiple materials, the limited spatial resolution of the discretized level-set function plays an important role. Under these circumstances the additive approach results in a top layer which is potentially concave at interfaces between two material regions (on the surface). The implicitly imposed concavity works well with the intrinsic geometry of a typical etching process, where a substrate is masked by a material with negligible etch rate. The substrate region is reduced and a concave surface is obtained. Hence, the multi-level-set approach is highly robust for etching simulations.

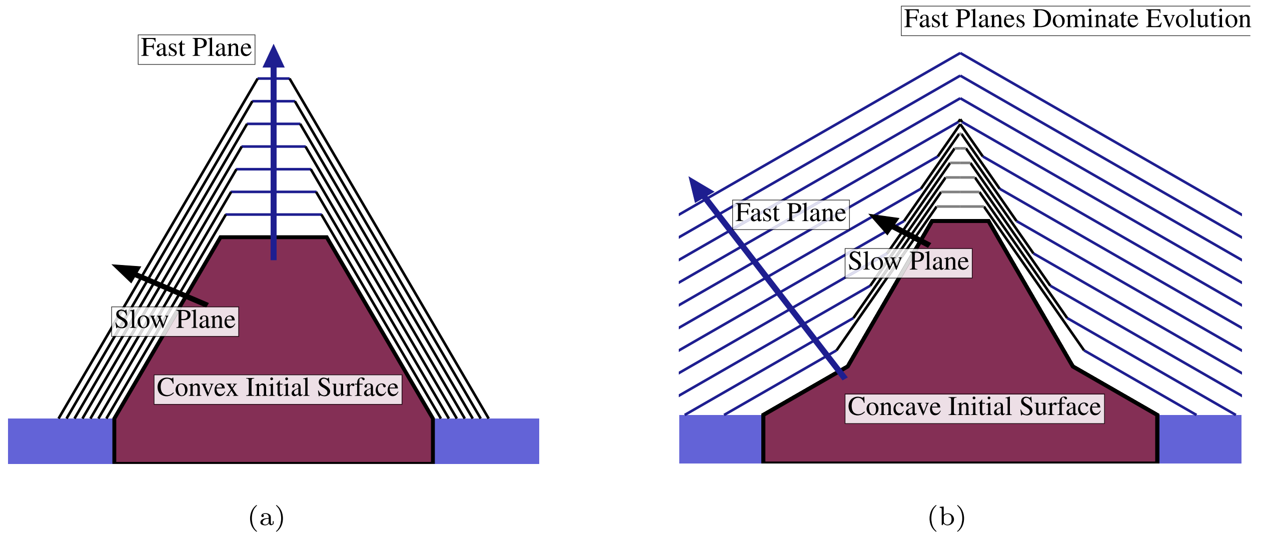

FIGURE 6. The convexity of an initial surface determines the epitaxial growth mode. The growth of convex initial geometries is dominated by the slowly growing crystallographic planes (a), while the growth of concave surfaces is dictated by the fast planes (b).

In contrast, selective deposition processes add new material regions to the domain and the intrinsic convexity depends on the initial condition. Convex and concave growth is both physically possible [20] and thus it is essential to ensure that the initial surface representation does not introduce artifacts caused by the limited spatial resolution. Fig. 6 illustrates the significant sensitivity of the final geometry on the initial state. In the case of convex growth, the slowly growing facets (planes) are dominating the temporal evolution, whereas the fast planes dominate for concave growth. Even if the exact same crystallographic growth rate distribution is used, i.e., the growth rate for every crystallographic direction has exactly the same value, the qualitative geometric shapes as shown in Fig. 6 can be observed. Thus, the time evolution of the crystal growth is not exclusively determined by the crystallographic directions.

In order to prevent the introduction of artifacts at material interfaces, we divide the initial top layer $\mathrm{TL_i}$, defined prior to a deposition step, into two subsets. One subset consists of all material regions which allow selective growth - denoted as E - and the other subset comprises regions associated with the union of all material regions which do not allow growth, referred to as *mask* M,

$$\mathrm{TL_i} = \mathrm{E} \cup \mathrm{M}. \tag{19}$$

We define the initial *deposition* top layer $\mathrm{TL_i^{Depo}}$ as

$$\mathrm{TL_i^{Depo}} = (\Omega \setminus \mathrm{TL_i}) \cup \mathrm{M}, \tag{20}$$

where Ω denotes the entire computational domain. Fig. 7a visualizes both top layers for a simple structure. In particular, the surface orientation of $\mathrm{TL_i^{Depo}}$ is inverted with respect to $\mathrm{TL_i}$,

ensuring a consistent orientation of the deposition top layer $\mathrm{TL^{Depo}}$ and the *mask* during the growth, which is essential for robust growth (Fig. 7b). After the surface advection the final top layer $\mathrm{TL_f^{Depo}}$ can be converted back to the traditional wrapping of the top layer with the boolean operation

$$\mathrm{TL_f} = \left(\Omega \setminus \mathrm{TL_f^{Depo}}\right) \cup \mathrm{TL_i}. \tag{21}$$

This conversion is performed after the epitaxial growth step, to return to the original layer wrapping described in (18). This is necessary, as other processing steps simulated subsequently depend on this material representation.

The impact of the deposition is illustrated in the configuration depicted in Fig. 8. SiGe is epitaxially grown on Si in order to fill a trench formed by oxide sidewalls. In this case, E refers to the level-set representation of the material regions which enable growth of SiGe. The *mask* M is the oxide region. Fig. 8a illustrates the temporal evolution if the initial top layer (dashed line, $\mathrm{TL_i}$) is constructed in the traditional way (19). The concave nature of $\mathrm{TL_i}$ causes problems at the oxide sidewalls. The direction of the normal vector associated with the grid point next to the corners (marked 'i' and 'ii') is not unambiguously defined. Even though a finite set of ambiguous level-set normals is generally not problematic for the level-set method [16], the speed function introduces a strong sensitivity to the normal orientation. At the initial time step, the normal at 'i' is associated with a slow growth rate, while the normal at 'ii' defines a growth rate which is even larger than R_{100}. This asymmetry is due to the non-symmetrical grid alignment which is the general case in a level-set simulation.[2] Consequently, concave growth

[2]Non-symmetrical grid alignment refers to the front (zero level-set), describing the cavity sidewalls, not being evenly spaced to the grid for both sidewalls. If a symmetrical grid alignment with the traditional top layer is enforced, the resulting topography evolution is symmetrical. However, front propagation is still highly sensitive to the direction of the normal vector associated with the grid point next to the corners ('i' and 'ii').

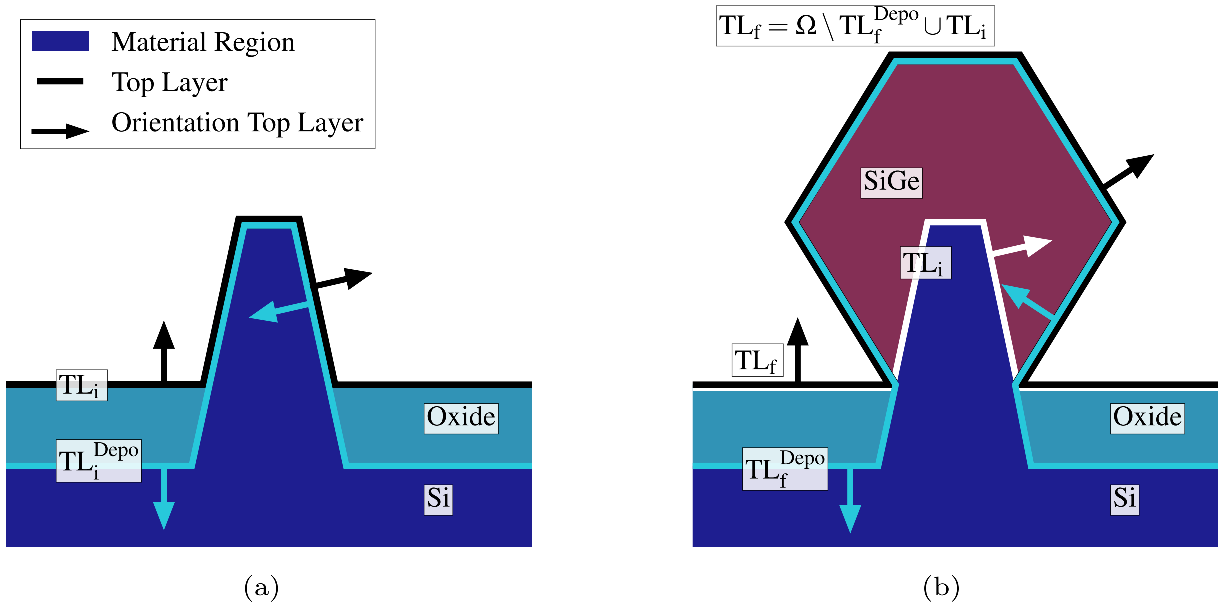

FIGURE 7. Illustration of the top layer approach for multiple regions during an epitaxial growth simulation. SiGe is heteroepitaxially grown on Si, but not on the oxide. (a) The traditional initial top layer TL_i circumscribes both Si and the oxide, while the deposition top layer TL_i^{Depo} excludes the oxide. Additionally, the orientation is flipped, ensuring consistent orientation of the deposition top layer TL^{Depo} and the *mask*. (b) TL_i^{Depo} enables robust growth and the final deposition top layer TL_f^{Depo} can be converted back to the traditional representation TL_f by applying boolean operations.

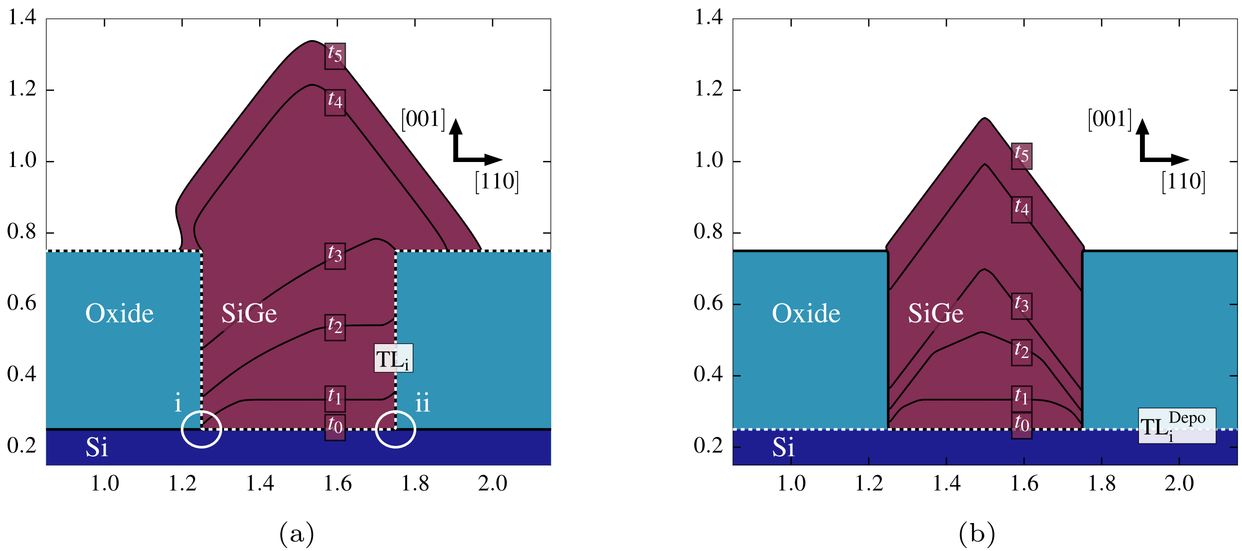

FIGURE 8. Temporal evolution of the simulated surface for hetereoepitaxial trenchfilling (growth rates SEG, as defined in Tab. 1) with (a) the traditional initial top layer resulting in incorrect results and (b) the deposition top layer (t_0 = 0s, t_2 = 2s, t_3 = 15s, t_4 = 50s, and t_5 = 67s, $\Delta x = 0.0045\mu m$). The local convexity implied by the discretized level-set field is critical at the multi-material interfaces 'i' and 'ii'. Distances are given in μm.

emerges, even though the physical initial situation requires convex growth. On the contrary, the deposition top layer TL_i^{Depo}, which is constructed employing (20), ensures convex and symmetrical growth (Fig. 8b).

IV. SIMULATION SETUP

We assess the capability of the proposed Stencil Lax-Friedrichs scheme by performing etching and non-planar epitaxy simulations. In this section, we present the two- and three-dimensional problem cases, the construction of the speed function, and describe the geometry parameters which are expected to emerge in the ideal case. Furthermore, multiple speed functions (associated with different etchants/growth conditions) are investigated. In order to investigate and validate the capability of our methods, we assume a set of etch/growth rates which result in realistic geometric shapes. The relative magnitude of the rates are motivated from experimental observations

and are used to construct speed functions which reflect commonly applied processing conditions. This allows us to define geometric parameters which are directly determined by the specified etch/growth rates as a reference for an ideal surface propagation. These parameters, such as the distance a crystal facet travels, have ideal values governed by the etch/growth rates and we compare them with our simulation results in Section V. All simulations are performed using the sparse field level-set based topography simulator `ViennaTS`. The sparse field level-set method is employed on a hierarchical run-length encoded (HRLE) level-set data structure [24] to enable fast and memory-efficient two- and three-dimensional topography simulation. The domain is equidistantly discretized and only grid points which are close to the interface (active grid points) are updated. In order to solve the level-set equation for all active grid points, the level-set values of neighboring grid points are expanded using Manhatten distance computations [21].

A. TWO-DIMENSIONAL WET ETCH

We evaluate the Stencil Lax-Friedrichs scheme by considering a planar two-dimensional wet etching configuration, as illustrated in Fig. 9. The planar substrate (Si) is partially masked leaving the substrate exposed to the wet chemical etchant (e.g., KOH) in the mask opening. We model the anisotropic etch rates using the linear Hubbard interpolation (Section II) between four etch rates along the crystallographic directions $\langle 100\rangle$, $\langle 110\rangle$, $\langle 111\rangle$, and $\langle 113\rangle$, resulting in a purely surface normal-dependent speed function of the form (2). Here, we consider etchants characterized by global minima in $\langle 111\rangle$ directions, which is the case for the commonly used etchants and etching conditions [25].

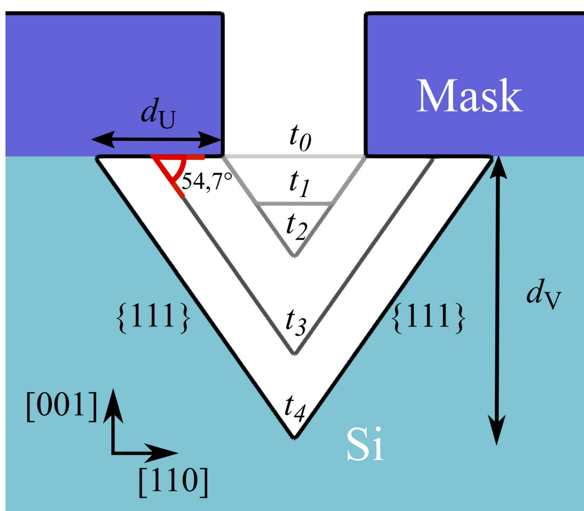

FIGURE 9. Schematic illustration of the wet etching experiment. The initially flat Si substrate (t_0) is etched, where the mask has an opening. The etchant (e.g., KOH) removes {111} planes with the slowest rate. Consequently, these planes define a V-shaped profile at t_2. For longer etch times the {111} planes slowly progress ($t_2 \to t_3 \to t_4$), defining a mask undercut d_U and depth of the V-tip d_V.

The temporal evolution shown in Fig. 9 starts from a planar initial substrate (t_0) and is characteristically defined by the limiting slow etch rate R_{111}, which results in the formation of a V-shaped profile (t_2). Once the V-shaped profile is formed, further etching proceeds very slowly ($t_3 - t_2 \gg t_2 - t_1$). Nevertheless, the {111} planes are gradually advected, resulting in a mask undercut d_U and profile depth d_V. These quantities are important geometric parameters in wet etching experiments and allow for the comparison of the simulation results with the ideal values: Assuming an etchant with minimum etch rates along $\langle 111\rangle$ (R_{111}) and a substrate oriented as given in Fig. 9, two {111} planes are formed. The angle α^{ideal} between the substrate surface and a {111} plane is $\arctan\sqrt{2} \approx 54.74°$. Elementary geometry operations provide the undercut distance after etch time t for a rate in $\langle 111\rangle$ direction R_{111}

$$d_U^{\text{ideal}} = \frac{1}{\sin\alpha} R_{111} t \approx 1.22\, R_{111} t. \tag{22}$$

Furthermore, with the assumption that the V-shaped profile has already been formed, the tip has moved by

$$d_V^{\text{ideal}} = \frac{1}{\cos\alpha} R_{111} t \approx 1.73\, R_{111} t. \tag{23}$$

We employ these distances and α to validate the accuracy of the proposed Stencil Lax-Friedrichs scheme in Section V-A.

B. THREE-DIMENSIONAL NON-PLANAR EPITAXY

In order to demonstrate the deposition top layer, we consider a three-dimensional fin structure, which forms the geometrical basis of modern FinFETs [5]. A crucial process step during the fabrication of a FinFET is heteroepitaxial growth of SiGe on top of the Si fin. The initial Si fin is illustrated in Fig. 10a, where half of the structure is shown. Similar to crystallographic wet etching, the growth rates of epitaxial SiGe are strongly anisotropic. Depending on the growth conditions (e.g., temperature, partial pressures), the relative magnitude of the growth rates differs [11]. In the following, we assume growth conditions resulting in a minimal growth rate along $\langle 111\rangle$ directions. Consequently, {111} facets dominate the growth of the crystal (convex initial geometry of the fin, c.f. Fig. 6) and a SiGe diamond on top of the Si fin is formed. Fig. 10b shows the fully formed SiGe diamond, which is characterized by the geometry parameters overgrowth height d_{OG} and the lateral length d_L. The ideal lateral length is determined by the angle ρ between the substrate surface and the bottom {111} planes ($\rho = \arctan\sqrt{2} \approx 54.74°$), the growth rate R_{111} along $\langle 111\rangle$, and the growth time t.

$$d_L^{\text{ideal}} = \frac{1}{\sin\rho} R_{111} t \approx 1.22\, R_{111} t \tag{24}$$

The ideal overgrowth height can be expressed in terms of d_L^{ideal} and the fin length d_{Fin}.

$$d_{OG}^{\text{ideal}} = \left(d_{\text{Fin}}/2 + d_L^{\text{ideal}}\right) \tan\rho \tag{25}$$

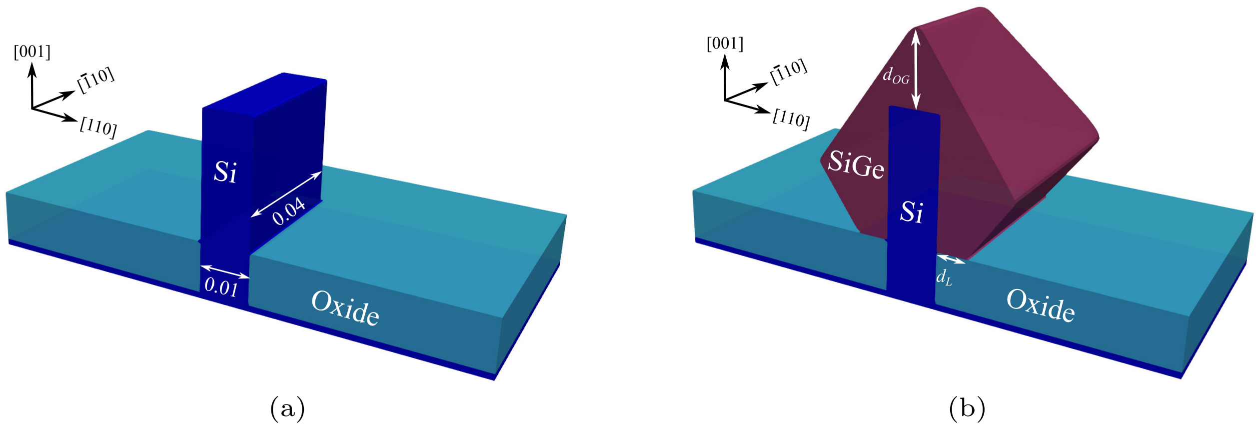

FIGURE 10. (a) Three-dimensional fin structure (length 10nm, width 80nm, and height 35nm) which is employed for epitaxial growth simulations. (b) SiGe is heteroepitaxially grown on Si forming {111} facets. Distances are given in μm.

TABLE 1. Etch rates and simulation results for two-dimensional 800s wet etching simulation (Fig. 9). The simulated mask undercut d_U and the V tip shift d_V compared with the ideal values $d_{U,V}^{ideal}$. In the case of the etchant SEG the V-shaped profile is not fully evolved before $T_0 = 83$s. The spatial resolution for the simulations is $\Delta x = 0.0045\mu$m.

	Rates (µm/ min)				Etch Times (s)		Distances (µm)				Relative Error	
Etchant	R_{100}	R_{110}	R_{111}	R_{113}	T	T_0	d_U	d_U^{ideal}	d_V	d_V^{ideal}	Δd_U	Δd_V
KOH	1.0	1.855	0.0073	1.801	800	0	0.122	0.119	0.172	0.169	0.587	0.830
SEG	0.5	0.2	0.05	0.25	800	83	0.732	0.731	1.035	1.033	0.321	0.321
T1	1.0	1.5	0.03	1.5	800	0	0.488	0.490	0.691	0.693	0.328	0.463
T2	1.0	0.6	0.05	0.9	800	0	0.815	0.816	1.152	1.155	0.392	0.554
T3	0.7	0.6	0.04	1	800	0	0.655	0.653	0.926	0.924	0.388	0.549

In Section V-C these geometry parameters serve as reference to demonstrate the capability of the deposition top layer approach.

V. RESULTS

In this section, we present simulation results for the two-dimensional wet etching and the three-dimensional heteroepitaxy setup introduced in Section IV. Furthermore, we discuss the impact of individual dissipation terms, the spatial resolution, and the time-stepping on the front propagation. Finally, we show the deposition top layer.

A. DISSIPATION TERMS AND SPATIAL RESOLUTION

The etching and epitaxy simulations considered in this study adopt several speed functions which involve the etch/growth rate combinations given in Tab. 1 and referred to as *etchants* in the following. The magnitude of the rates is motivated by experimental studies [11], [25], [31], which provides a realistic picture of the typically encountered rate ratios R_{111}/R_{100}, R_{111}/R_{110}, etc. for different directions. These rates are only applied if the active material is Si. The etch rate of the mask is negligible and thus set to zero in this study. Fig. 11 visualizes the results of a 800s wet etching process for the two-dimensional geometry presented in Section IV. All etchants lead to the characteristic V-shaped-profile with a specific mask undercut d_U and tip depth d_V. These distances are evaluated by extrapolating the final {111} lines and intersecting the resulting straight lines with the mask-silicon interface (d_U) and with themselves (d_V), respectively. The results presented in Tab. 1 demonstrate the high accuracy of the simulations, which is validated with the relative error metric

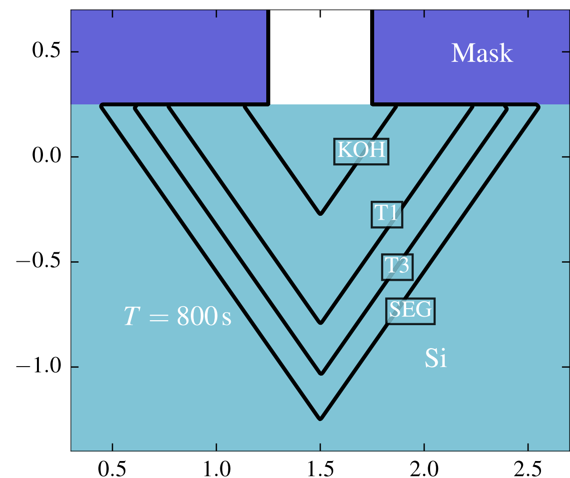

FIGURE 11. Simulation results for the two-dimensional wet etching setup (Fig. 9) employing several etchants (Tab. 1). The etch time is $T = 800$s and the spatial resolution is $\Delta x = 0.0045\mu$m. The resulting geometry displays the characteristic {111} planes, forming a V-shaped profile. Distances are given in μm.

$$\Delta d_U = \frac{|d_U^{ideal} - d_U|}{\Delta x} \tag{26}$$

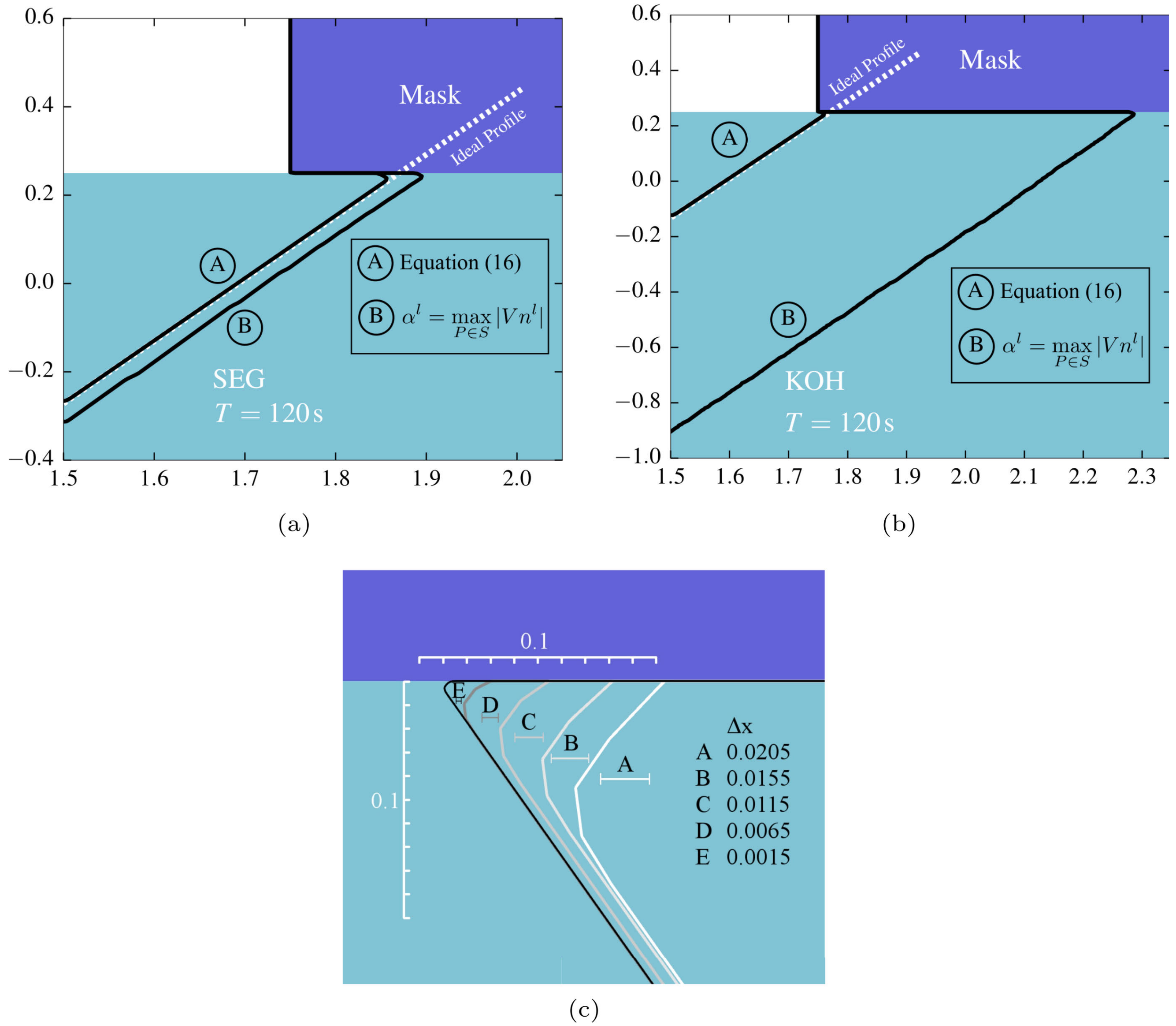

FIGURE 12. Comparison of the impact of the dissipation coefficients on the simulated etch front after 120s for (a) etchant KOH and (b) etchant SEG. (16) results in high accuracy fronts (label A) with respect to the ideal profile. If only the elemental term Vn^l is considered the propagation is instable resulting in noisy fronts (label B). This is the case even though the advanced adaptive time-stepping (17) is employed. The magnitude of the error strongly depends on the etchant. (c) The Stencil Lax-Friedrichs scheme introduces rounding which extends over approximately 3 grid spacings. All distances are given in μm.

and an equivalent definition for Δd_{V}. (26) measures the cumulative spatial error of the wet etching test simulations, which comprise more than 1000 time steps. Hence, a resulting $\Delta d_{\mathrm{U,V}}$ smaller than 1.0, i.e., the spatial error is less than the grid resolution, indicates excellent accuracy.

The high accuracy is made possible by the evaluation of all terms associated with the partial derivative of the Hamiltonian as given in (14). In particular, the terms involving $\partial V/\partial n^l$ are required to enable a stable front propagation, as demonstrated in Fig. 12a and Fig. 12b. The dissipation terms added to the Hamiltonian (8) introduce rounding of corners present in the front. In order to study the rounding we compare the simulated front directly beneath the mask for different spatial resolutions ranging from $\Delta x = 0.0205$ to $\Delta x = 0.0015$. Fig. 12c demonstrates that the proposed dissipation scheme causes rounding extending over roughly three grid cells, which holds true for $\Delta x \to 0$.

B. TIME STEPPING

In our implementation, we extend the calculation of the final time step Δt for the explicit time integration (9). In the traditional implementation, the time step is calculated according to

$$\Delta t^{\mathrm{F}} = \min\left(\frac{C_{\mathrm{CFL}}}{\max|\hat{H}|}, \Delta t^{L}\right). \tag{27}$$

TABLE 2. Undercut and V-tip distances (d_U and d_V, respectively) for two-dimensional simulations of 800s wet etching. The results obtained from traditional time-stepping (employing different CFL numbers C_{CFL}) and from advanced adaptive time-stepping (17) are compared with the ideal distances (relative error (26)). Entries indicated with ⋆ refer to simulations that drifted out of the simulation domain (due to severe instable front propagation).

Etchant	C_{CFL}	Distances (µm) d_U	d_V	Relative Error Δd_U	Δd_V	Etchant	C_{CFL}	Distances (µm) d_U	d_V	Relative Error Δd_U	Δd_V
KOH	0.5	⋆	⋆	⋆	⋆	SEG	0.5	0.732	1.036	0.070	0.220
$\Delta x = 0.0105$	0.3	0.611	0.886	46.850	68.280	$\Delta x = 0.0105$	0.3	0.731	1.035	0.030	0.160
	0.1	0.247	0.353	12.153	17.519		0.1	0.731	1.035	0.001	0.110
	0.05	0.133	0.189	1.356	1.918		0.05	0.731	1.035	0.001	0.110
	0.03	0.135	0.191	1.543	2.182		0.03	0.731	1.034	0.010	0.100
	0.01	0.122	0.173	0.295	0.421		0.01	0.731	1.034	0.010	0.100
	Adaptive	0.118	0.166	0.159	0.225		Adaptive	0.731	1.036	0.060	0.200
	Ideal	0.119	0.169				Ideal	0.731	1.039		
KOH	0.5	⋆	⋆	⋆	⋆	T2	0.5	⋆	⋆	⋆	⋆
$\Delta x = 0.0045$	0.3	0.622	0.905	111.703	163.577	$\Delta x = 0.0045$	0.3	0.986	1.446	46.308	75.069
	0.1	0.195	0.278	16.893	24.245		0.1	0.815	1.152	0.512	0.695
	0.05	0.154	0.218	7.695	10.883		0.05	0.814	1.151	0.877	0.532
	0.03	0.134	0.190	3.268	4.719		0.03	0.814	1.151	0.881	1.246
	0.01	0.122	0.174	0.527	1.161		0.01	0.814	1.151	0.884	1.250
	Adaptive	0.122	0.172	0.587	0.830		Adaptive	0.815	1.152	0.392	0.554
	Ideal	0.119	0.169				Ideal	0.816	1.155		

The first argument of the minimum operation is the CFL condition [17], where the maximum value of $\hat{H}$ is evaluated over the set of active grid points. This condition ensures that the surface is advanced at most one grid spacing per time step. Δt^L refers to a time step which ensures correct etching simulation in presence of multiple layers [21]. In order to satisfy the monotonicity condition (10), this calculation is extended by evaluating (17), resulting in Δt^{D}. Thus, the final Δt, fulfilling the traditional conditions and the monotonicity condition, is

$$\Delta t = \min\left(\Delta t^{\mathrm{F}}, \Delta t^{\mathrm{D}}\right). \quad (28)$$

Compared to the traditional implementation, (17) reduces the effective time step in order to achieve stable front propagation. We demonstrate the impact of the time step reduction by investigating the results for simulations with and without resorting to (17). In the first case, there is no associated CFL parameter, thus we perform the simulations with the maximum CFL parameter values beneficial for the sparse field method, i.e., $C_{\mathrm{CFL}} = 0.5$ [17]. Using this value enforces that only the level-set values of active grid points can change their sign during one time step, which leads to guaranteed robust advection. In the latter case (i.e., without resorting to (17)), we employ values for C_{CFL} from 0.5 to 0.01, where smaller values imply smaller time steps Δt. Tab. 2 demonstrates the impact of the etchant, the spatial resolution, and C_{CFL} on the accuracy of the front propagation. The spatial accuracy after an 800s etching simulation with the respective etchant is assessed using the distances d_{U} and d_{V} (Fig. 9), which are compared to the ideal distances by means of the relative error metric (26).

Tab. 2 demonstrates the significance of the *nature* of the speed function for the time-stepping. In the traditional time step calculation, the etchant KOH requires $C_{\mathrm{CFL}} = 0.01$ to fulfill the high accuracy criterion $\Delta d_{\mathrm{U,V}} < 1.0$. In contrast, $C_{\mathrm{CFL}} = 0.5$ results in excellent accuracy for etchant SEG, while etchant T2 requires $C_{\mathrm{CFL}} = 0.1$ for accurate results. Consequently, the stability of the traditional implementation can only be guaranteed if the appropriate C_{CFL} is known *a-priori* which is not the case for general etchants, i.e., speed function. The results indicated with *Adaptive* originate from the implementation with the additional (17) and demonstrate the capability of the proposed scheme to achieve high accuracy.

We further investigate the time-stepping approach by analyzing the individual steps Δt taken during the test simulation. Fig. 13a depicts the distribution of Δt associated with the etchant KOH and $C_{\mathrm{CFL}} = 0.01$ for the traditional and the proposed adaptive implementation. The traditional implementation shows a broad distribution of Δt with two distinctive peaks, while the adaptive scheme exhibits a significantly narrower distribution. The distribution of Δt over time is illustrated in Fig. 13b and demonstrates that the traditional scheme leads to strong fluctuations in Δt. These can be attributed to the non-convex *nature* of the speed function, which causes fluctuations in the velocities associated with the active grid points. The maximum velocity and hence Δt (27) depends on the exact position of the front relative to the grid, causing variations in Δt, which might span more than three orders of magnitude. Furthermore, the two distinctive peaks arise due to the structural change in the topography. Before the V-shaped profile is formed ($t < t_2$ in Fig. 9), small time steps dominate, but as soon as the etch front slowly undercuts the mask, fluctuations in the maximum velocity arise. Hence, reducing the C_{CFL} to considerably small values does not resolve the root cause of the fluctuations. In contrast,

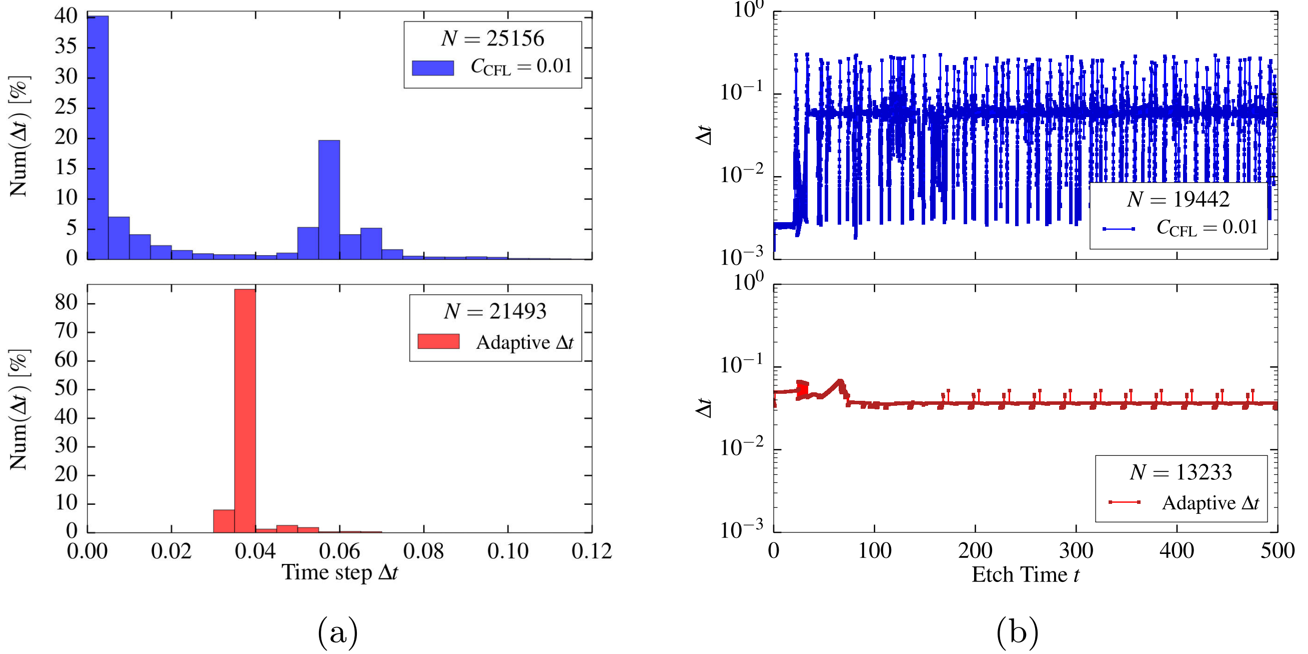

FIGURE 13. (a) Distribution of the time step Δt in 800s wet etching simulations (KOH, $\Delta x = 0.0045$). N refers to the total number of time steps. The traditional time-stepping (top) with a C_{CFL} which enables results of acceptable accuracy shows a broad distribution of Δt with two distinctive peaks. By contrast, the advanced adaptive time-stepping (bottom) results in a narrow distribution. (b) Temporal evolution of Δt for the first 500s. The traditional time-stepping (top) shows oscillations which originate from the strongly varying speed values in the proximity of the V-shaped corner (Fig. 5d). By contrast, the advanced adaptive time-stepping (bottom) reduces the time step if high values of dissipation are needed. Thus, the fluctuation of Δt is significantly reduced. Furthermore, the evolution of Δt shows divergent behavior for the first portion of the etching simulations. This is caused by the gradual evolution of the V-shape and the mask undercut, which requires the formation of the acute angle of the front beneath the Si-mask interface (shown in Fig. 12c). Once the acute angle is formed, the undercut proceeds in a regular way, with periodical fluctuations in the advanced adaptive time steps (bottom) being caused by the grid periodicity.

the advanced adaptive time-stepping strongly reduces the fluctuation of Δt, indicating that the front propagates in a numerically stable way.

C. NON-PLANAR DEPOSITION USING THE DEPOSITION TOP LAYER

In order to demonstrate the capability of the deposition top layer, we consider the three-dimensional fin structure illustrated in Fig. 10a. The epitaxial growth of SiGe on Si is modeled by employing the growth rates SEG, as given in Tab. 1. The fin structure consists of two material regions, oxide and Si. When determining the deposition top layer, we incorporate the information that oxide does not allow epitaxial growth of SiGe, in accordance with the discussion in Section III. Hence, we employ (20) with M being the oxide region. The resulting deposition top layer has qualitatively the same shape and orientation as the two-dimensional schematic illustration in Fig. 7a. In particular, the deposition top layer comprises the interface between oxide and Si. Furthermore, we use the Stencil Lax-Friedrichs scheme with advanced adaptive time-stepping to enable a stable front propagation. After the epitaxy process the final deposition top layer (cf. Fig. 7b) is converted back to the conventional one.

The resulting topography, visualized as triangulated mesh in Fig. 10b, shows the characteristic {111} facets formed by the epitaxially grown SiGe. The temporal evolution is illustrated in Fig. 14 for two slices: one along the Si fin (Fig. 14a) and one perpendicular to the fin (Fig. 14b). Starting from the rectangular structure imposed by the Si fin, the slowly growing {111} planes gradually dominate, until they are fully formed at $t = t_4$. The subsequent growth proceeds according to R_{111}, which results in effective lateral growth along the oxide region analogously to the mask undercut in the etching test case. The lateral growth distance after $t_5 = 10$s is $d_{\text{L}} = 0.01\mu$m, yielding a relative spatial error of $\Delta d_{\text{L}} = 0.344$. The overgrowth height d_{OG} is 0.021μm. Additionally, we assess the quality of the simulated planes by comparing the angles α, β, γ, and δ illustrated in Fig. 14 with the angles between the ideal crystallographic facets. The results presented in Tab. 3 show the high accuracy of the simulated facets.

TABLE 3. Simulated and ideal angles and distances, as indicated in Fig. 14, for a 10s hetereoepitaxy simulation employing SEG growth rates. The ideal angles are obtained by calculating the angles between the ideal {111} and {100} planes, while ideal distances are calculated using (24) and (25).

	Angles (°)				Distances (μm)	
	α	β	γ	η	d_{L}	d_{OG}
Ideal	109.5	70.53	125.3	54.74	0.01	0.02
Simulated	109.5	70.53	125.3	54.73	0.01	0.02

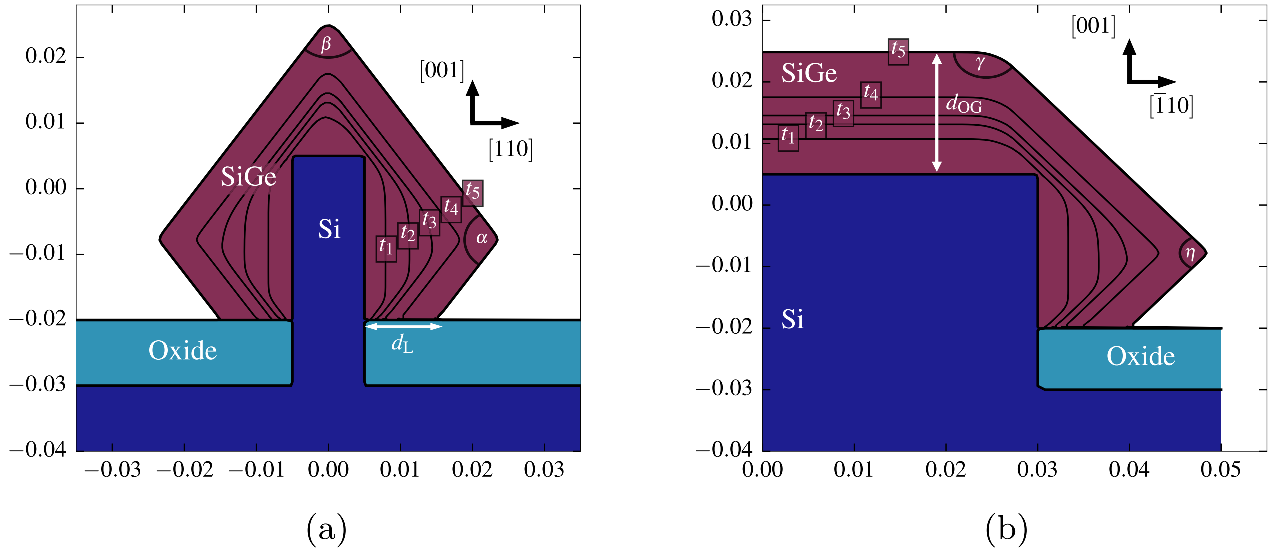

FIGURE 14. Temporal evolution of heteroepitaxial growth with the SEG growth rate model (Tab. 1). Slices of the topography (a) along the fin and (b) perpendicular to the fin are depicted for a resolution of $\Delta x = 6 \times 10^{-4}\,\mu$m, $t_1 = 1$s, $t_2 = 2$s, $t_3 = 3$s, $t_4 = 5$s, and $t_5 = 10$s. The angles indicated by α, β, γ, and δ are compared with the ideal values in Tab. 3. Distances are given in μm.

VI. SUMMARY

We presented numerical methods to enable accurate and robust level-set based simulation of anisotropic wet etching and non-planar epitaxy. These semiconductor fabrication processes are characterized by highly crystal orientation-sensitive etch/growth rates. The level-set equation describing the motion of the wafer surface involves non-convex Hamiltonians which potentially cause instable front propagation. We proposed a stability-providing Stencil Lax-Friedrichs scheme with dissipation coefficients and advanced adaptive time-stepping, tailored to the purely normal-dependent etching and epitaxy speed functions. The scheme does not rely on numerical calibration parameters and is thus applicable for a variety of etchants and material combinations. Furthermore, we introduce the deposition top layer approach which is a method to robustly handle multiple material regions in non-planar epitaxy simulations. The deposition top layer ensures that the discretized level-set representation of the initial topography prior to an epitaxy step respects the convexity of the initial configuration.

The capabilities of the Stencil Lax-Friedrichs scheme and the deposition top layer approach have been demonstrated by simulating two- and three-dimensional anisotropic wet etching and non-planar epitaxy processes as used in industry. The schemes have been implemented using the open-source topography simulator `ViennaTS`. Simulations of several etch/growth conditions resulting in different speed functions, have performed. The final topographies have been compared to the ideal geometries and the high accuracy of the results have been confirmed. Furthermore, the impact of individual dissipation terms, the spatial resolution, and the advanced adaptive time-stepping have been investigated.

APPENDIX A
DERIVATION OF EQUATION (14)

We calculate the partial derivative $\partial H/\partial \phi_l$ with $l \in \{x, y, z\}$ under the assumption of a speed function of the form (2). Hence, the speed function V is a function of only the surface normal vector components n^l. In the level-set method the normal vector can be expressed in terms of the spatial partial derivatives of ϕ, as presented in (3). Thus, n^l can be written in terms of ϕ_l as

$$n^l = \frac{\phi_l}{\|\nabla\phi\|} = \frac{\phi_l}{\sqrt{\phi_x^2 + \phi_y^2 + \phi_z^2}}. \tag{29}$$

As a consequence, V has the form

$$V = V(n^x(\phi_x, \phi_y, \phi_z), n^y(\phi_x, \phi_y, \phi_z), n^z(\phi_x, \phi_y, \phi_z)). \tag{30}$$

In the following, we present the calculation of $\partial H/\partial \phi_x$. The remaining expressions $\partial H/\partial \phi_y$ and $\partial H/\partial \phi_z$ can be derived analogously. Applying the product rule of differentiation yields

$$\frac{\partial H}{\partial \phi_x} = \frac{\partial}{\partial \phi_x} V\|\nabla\phi\| = \frac{\partial V}{\partial \phi_x}\|\nabla\phi\| + V\frac{\partial\|\nabla\phi\|}{\partial \phi_x}. \tag{31}$$

First, we consider $\partial V/\partial \phi_x$ and employ the chain rule of differentiation.

$$\frac{\partial V}{\partial \phi_x} = \frac{\partial V}{\partial n^x}\frac{\partial n^x}{\partial \phi_x} + \frac{\partial V}{\partial n^y}\frac{\partial n^y}{\partial \phi_x} + \frac{\partial V}{\partial n^z}\frac{\partial n^z}{\partial \phi_x} \tag{32}$$

The expressions $\partial n^l/\partial \phi_x$ can be evaluated by making use of (29).

$$\frac{\partial V}{\partial \phi_x} = \frac{1}{\|\nabla\phi\|^3}\left[\frac{\partial V}{\partial n^x}\left(\phi_y^2 + \phi_z^2\right) - \frac{\partial V}{\partial n^y}\phi_x\phi_y - \frac{\partial V}{\partial n^z}\phi_x\phi_z\right] \tag{33}$$

Secondly, $\partial\|\nabla\phi\|/\partial\phi_x$ is expressed in terms of n^x.

$$\frac{\partial\|\nabla\phi\|}{\partial\phi_x} = \frac{\phi_x}{\|\nabla\phi\|} = n^x \tag{34}$$

We apply these intermediate results to (31), which yields

$$\frac{\partial H}{\partial\phi_x} = \frac{\partial V}{\partial n^x}\frac{\phi_y^2+\phi_z^2}{\|\nabla\phi\|^2} - \frac{\partial V}{\partial n^y}\frac{\phi_x\phi_y}{\|\nabla\phi\|^2} - \frac{\partial V}{\partial n^z}\frac{\phi_x\phi_z}{\|\nabla\phi\|^2} + Vn^x. \tag{35}$$

The results of the analogous calculations for $\partial H/\partial\phi_y$ and $\partial H/\partial\phi_z$ have the same structure, leading to (14).

REFERENCES

[1] H. Geng, *Semiconductor Manufacturing Handbook*. New York, NY, USA: McGraw-Hill, 2017.

[2] J. Shen, D. Zhang, Y. Wang, and Y. Gan, "AFM and SEM study on crystallographic and topographical evolution of wet-etched patterned sapphire substrates (PSS): I. Cone-shaped PSS etched in sulfuric acid and phosphoric acid mixture (3:1) at 230°C," *ECS J. Solid State Sci. Technol.*, vol. 6, no. 1, pp. R24–R34, 2017, doi: 10.1149/2.0221701jss.

[3] H.-C. Lo, J. Peng, E. Reis, B. Zhu, W. Ma, S. Y. Mun, S. Shintri, E. M. Bazizi, C. Gaire, Y. Qi, J. Chen, S. N. Ting, O. Hu, and S. Samavedam, "A novel approach to control source/drain cavity profile for device performance improvement," *IEEE Trans. Electron Devices*, vol. 65, no. 9, pp. 3640–3645, Sep. 2018, doi: 10.1109/ted.2018.2856770.

[4] C. Qin, H. Yin, G. Wang, P. Hong, X. Ma, H. Cui, Y. Lu, L. Meng, H. Yin, H. Zhong, J. Yan, H. Zhu, Q. Xu, J. Li, C. Zhao, and H. H. Radamson, "Study of sigma-shaped source/drain recesses for embedded-SiGe pMOSFETs," *Microelectronic Eng.*, vol. 181, pp. 22–28, Sep. 2017, doi: 10.1016/j.mee.2017.07.001.

[5] J. Peng, Y. Qi, H.-C. Lo, P. Zhao, C. Yong, J. Yan, X. Dou, H. Zhan, Y. Shen, S. Regonda, O. Hu, H. Yu, M. Joshi, C. Adams, R. Carter, and S. Samavedam, "Source/drain eSiGe engineering for FinFET technology," *Semicond. Sci. Technol.*, vol. 32, no. 9, Sep. 2017, Art. no. 094004, doi: 10.1088/1361-6641/aa7d3f.

[6] S. Barraud *et al.*, "Vertically stacked-nanowires MOSFETs in a replacement metal gate process with inner spacer and SiGe source/drain," in *IEDM Tech. Dig.*, Dec. 2016, pp. 17.6.1–17.6.4, doi: 10.1109/IEDM.2016.7838441.

[7] S. Barraud *et al.*, "Tunability of parasitic channel in gate-all-around stacked nanosheets," in *IEDM Tech. Dig.*, Dec. 2018, pp. 21.3.1–21.3.4, doi: 10.1109/iedm.2018.8614507.

[8] S. Osher and J. A. Sethian, "Fronts propagating with curvature-dependent speed: Algorithms based on Hamilton-Jacobi formulations," *J. Comput. Phys.*, vol. 79, no. 1, pp. 12–49, Nov. 1988, doi: 10.1016/0021-9991(88)90002-2.

[9] F. Gibou, R. Fedkiw, and S. Osher, "A review of level-set methods and some recent applications," *J. Comput. Phys.*, vol. 353, pp. 82–109, Jan. 2018, doi: 10.1016/j.jcp.2017.10.006.

[10] J. A. Sethian, *Level Set Methods and Fast Marching Methods: Evolving Interfaces in Computational Geometry, Fluid Mechanics, Computer Vision, and Materials Science*, vol. 3. Cambridge, U.K.: Cambridge Univ. Press, 1999.

[11] D. Dutartre, A. Talbot, and N. Loubet, "Facet propagation in Si and SiGe epitaxy or etching," *ECS Trans.*, vol. 3, no. 7, pp. 473–487, Dec. 2019, doi: 10.1149/1.2355845.

[12] H. Seidel, L. Csepregi, A. Heuberger, and H. Baumgärtel, "Anisotropic etching of crystalline silicon in alkaline solutions: I. Orientation dependence and behavior of passivation layers," *J. Electrochem. Soc.*, vol. 137, no. 11, pp. 3612–3626, 1990, doi: 10.1149/1.2086277.

[13] E. Steinsland, T. Finstad, and A. Hanneborg, "Etch rates of (100), (111) and (110) single-crystal silicon in TMAH measured *in situ* by laser reflectance interferometry," *Sens. Actuators A, Phys.*, vol. 86, nos. 1–2, pp. 73–80, Oct. 2000, doi: 10.1016/s0924-4247(00)00309-5.

[14] B. Radjenović, J. K. Lee, and M. Radmilović-Radjenović, "Sparse field level set method for non-convex Hamiltonians in 3D plasma etching profile simulations," *Comput. Phys. Commun.*, vol. 174, no. 2, pp. 127–132, Jan. 2006, doi: 10.1016/j.cpc.2005.09.010.

[15] J. A. Sethian and D. Adalsteinsson, "An overview of level set methods for etching, deposition, and lithography development," *IEEE Trans. Semicond. Manuf.*, vol. 10, no. 1, pp. 167–184, Feb. 1997, doi: 10.1109/66.554505.

[16] S. Osher and R. Fedkiw, *Level Set Methods and Dynamic Implicit Surfaces*. New York, NY, USA: Springer-Verlag, 2003.

[17] O. Ertl, "Numerical methods for topography simulation," Doctoral dissertation, TU Wien, Vienna, Austria, 2010. [Online]. Available: http://www.iue.tuwien.ac.at/phd/ertl/

[18] C. Montoliu, N. Ferrando, M. A. Gosálvez, J. Cerdá, and R. J. Colom, "Implementation and evaluation of the level set method: Towards efficient and accurate simulation of wet etching for microengineering applications," *Comput. Phys. Commun.*, vol. 184, no. 10, pp. 2299–2309, Oct. 2013, doi: 10.1016/j.cpc.2013.05.016.

[19] D. Du, D. J. Srolovitz, M. E. Coltrin, and C. C. Mitchell, "Systematic prediction of kinetically limited crystal growth morphologies," *Phys. Rev. Lett.*, vol. 95, no. 15, Oct. 2005, Art. no. 155503, doi: 10.1103/physrevlett.95.155503.

[20] Q. Sun, C. D. Yerino, B. Leung, J. Han, and M. E. Coltrin, "Understanding and controlling heteroepitaxy with the kinetic Wulff plot: A case study with GaN," *J. Appl. Phys.*, vol. 110, no. 5, Sep. 2011, Art. no. 053517, doi: 10.1063/1.3632073.

[21] O. Ertl and S. Selberherr, "A fast level set framework for large three-dimensional topography simulations," *Comput. Phys. Commun.*, vol. 180, no. 8, pp. 1242–1250, Aug. 2009, doi: 10.1016/j.cpc.2009.02.002.

[22] *ViennaTS*. Accessed: Nov. 29, 2019. [Online]. Available: http://www.iue.tuwien.ac.at/software/viennats/

[23] R. T. Whitaker, "A level-set approach to 3D reconstruction from range data," *Int. J. Comput. Vis.*, vol. 29, no. 3, pp. 203–231, 1998, doi: 10.1023/A:1008036829907.

[24] B. Houston, M. B. Nielsen, C. Batty, O. Nilsson, and K. Museth, "Hierarchical RLE level set: A compact and versatile deformable surface representation," *ACM Trans. Graph.*, vol. 25, no. 1, pp. 151–175, Jan. 2006, doi: 10.1145/1122501.1122508.

[25] M. A. Gosálvez, P. Pal, and K. Sato, "Reconstructing the 3D etch rate distribution of silicon in anisotropic etchants using data from vicinal 1 0 0, 1 1 0 and 1 1 1 surfaces," *J. Micromech. Microeng.*, vol. 21, no. 10, Oct. 2011, Art. no. 105018, doi: 10.1088/0960-1317/21/10/105018.

[26] T. J. Hubbard, "MEMS design: The geometry of silicon micromachining," Ph.D. dissertation, California Inst. Technol., Pasadena, CA, USA, 1994. [Online]. Available: https://thesis.library.caltech.edu/3565/1/Hubbard_tj_1994.pdf

[27] M. G. Crandall and P.-L. Lions, "Viscosity solutions of Hamilton-Jacobi equations," *Trans. Amer. Math. Soc.*, vol. 277, no. 1, pp. 1–42, 1983, doi: 10.1090/S0002-9947-1983-0690039-8.

[28] M. G. Crandall and P. L. Lions, "Two approximations of solutions of Hamilton-Jacobi equations," *Math. Comput.*, vol. 43, no. 167, pp. 1–19, 1984, doi: 10.1090/S0025-5718-1984-0744921-8.

[29] W. T. Vetterling, S. A. Teukolsky, W. H. Press, and B. P. Flannery, *Numerical Recipes*. Cambridge, U.K.: University Press, 1989.

[30] R. Courant, K. Friedrichs, and H. Lewy, "Über die partiellen Differenzengleichungen der mathematischen Physik," *Math. Annalen*, vol. 100, no. 1, pp. 32–74, Dec. 1928, doi: 10.1007/BF01448839.

[31] H. Hirayama, M. Hiroi, and T. Ide, "311 facets of selectively grown epitaxial Si layers on SiO_2-patterned Si(100) surfaces," *Phys. Rev. B, Condens. Matter*, vol. 48, no. 23, pp. 17331–17337, Dec. 1993, doi: 10.1103/physrevb.48.17331.

ALEXANDER TOIFL received the bachelor's degree in electrical engineering and the master's degree in microelectronics and photonics from TU Wien, Austria, in 2016 and 2018, respectively, where he is currently pursuing the Ph.D. degree in process TCAD with the Institute for Microelectronics.

MICHAEL QUELL received the bachelor's and master's degrees in technical mathematics from TU Wien, Austria, in 2016 and 2018, respectively, where he is currently pursuing the Ph.D. degree in high performance algorithms and data structures for process TCAD with the Institute for Microelectronics.

XAVER KLEMENSCHITS received the M.Sc. degree in physics from the University of Birmingham, U.K., in 2017. He is currently pursuing the Ph.D. degree in process TCAD with the Institute of Microelectronics, TU Wien, Austria, in 2016. His research interests include data structures, computational frameworks, and physical models for high-performance process simulation.

PAUL MANSTETTEN received the Dipl.-Ing. degree in mechatronics from the Regensburg University of Applied Sciences, the M.Sc. degree in computational engineering from the University of Erlangen-Nuremberg, and the Ph.D. degree from the Institute for Microelectronics, TU Wien, Vienna, Austria, in 2018. He is currently a Postdoctoral Researcher with the Institute for Microelectronics, TU Wien, where he is working on high performance methods for semiconductor process simulation.

ANDREAS HÖSSINGER is currently an Engineering Manager in process simulation with the TCAD Division, Silvaco Europe Ltd., U.K., which is a leading provider of simulation software for the microelectronics industry. He has coauthored over 60 papers in journals and conferences.

SIEGFRIED SELBERHERR (Fellow, IEEE) is currently a Chair Professor with the Institute for Microelectronics, TU Wien, Austria. He has authored over 460 papers in journals and books. His research team has achieved over 1150 articles in conference proceedings.

JOSEF WEINBUB (Member, IEEE) is currently an Assistant Professor with the Institute for Microelectronics, TU Wien, Austria, where he leads the Christian Doppler Laboratory for High Performance TCAD. He has coauthored 12 proceedings books, over 50 articles in journals and books, and over 100 conference contributions.